

# Quantitative second harmonic generation imaging and modeling of the optical clearing mechanism in striated muscle and tendon

**Ronald LaComb**  
**Oleg Nadiarykh**

University of Connecticut Health Center  
Department of Cell Biology  
Center for Cell Analysis and Modeling  
Farmington, Connecticut 06030

**Shawn Carey**

Worcester Polytechnic Institute  
Department of Biomedical Engineering  
Worcester  
Massachusetts 01609

**Paul J. Campagnola**

University of Connecticut Health Center  
Department of Cell Biology  
Center for Cell Analysis and Modeling  
Farmington, Connecticut 06030

**Abstract.** We have investigated the mechanisms and capabilities of optical clearing in conjunction with second harmonic generation (SHG) imaging in tendon and striated muscle. Our approach combines three-dimensional (3-D) SHG imaging of the axial attenuation and directional response with Monte Carlo simulation (based on measured bulk optical properties) of the creation intensity and propagation through the tissues. Through these experiments and simulations, we show that reduction of the primary filter following glycerol treatment dominates the axial attenuation response in both muscle and tendon. However, these disparate tissue types are shown to clear through different mechanisms of the glycerol-tissue interaction. In the acellular tendon, glycerol application reduces scattering by both index matching as well as increasing the interfibril separation. This results in an overall enhancement of the 3-D SHG intensity, where good agreement is found between experiment and simulation. Through analysis of the axial response as a function of glycerol concentration in striated muscle, we conclude that the mechanism in this tissue arises from matching of the refractive index of the cytoplasm of the muscle cells with that of the surrounding higher-index collagenous perimysium. We further show that the proportional decrease in the scattering coefficient  $\mu_s$  with increasing glycerol fraction can be well-approximated by Mie theory. © 2008 Society of Photo-Optical Instrumentation Engineers. [DOI: 10.1117/1.2907207]

**Keywords:** second-harmonic generation; multiple scattering; tissues; image acquisition/recording; microscopy; mie theory.

Paper 07427SSR received Oct. 17, 2007; revised manuscript received Feb. 4, 2008; accepted for publication Feb. 8, 2008; published online Apr. 21, 2008.

## 1 Introduction

There has been considerable recent interest in high-resolution optical imaging of tissue structure for diagnostic and clinical applications. As pioneered by Chance,<sup>1</sup> tissue properties have most commonly been assessed through the use of photon migration studies. More recently such efforts have evolved into diffuse optical tomography methods for *in vivo* imaging.<sup>2-6</sup> These approaches can obtain scattering, absorption, and fluorescence data in tissue through depths of a few centimeters in thickness, and thus provide valuable assays in diagnosing pathologies such as breast cancer. However, these techniques are limited in resolution to  $\sim 1$  mm, and it is increasingly recognized that changes in the microscopic tissue structure, e.g., the collagen fibril assembly in and around tumors, may also be early indicators of disease. Higher resolution is obtainable through multiphoton microscopy (MPM) and optical coherence tomography (OCT), and these techniques provide their own respective pieces of information on tissue assembly. Al-

though both these modalities typically use near-infrared wavelengths (700 to 1000 nm), due to the highly scattering nature of tissues, they are still limited to probing through depths of thickness  $< 1$  mm. While this is sufficient for examining *ex vivo* tissues or superficial tissues such as skin *in vivo*, a variety of organ imaging applications require deeper penetration.

To help overcome this limitation, several researchers have recently employed the optical clearing method, where a high-refractive-index, hyperosmotic reagent (e.g., glycerol, sugars, or sugar alcohols) is added to the tissue to increase its transparency. Such diverse tissues as skin,<sup>7-9</sup> blood,<sup>10</sup> *dura mater*,<sup>11</sup> gastric tissue,<sup>12</sup> sclera,<sup>13</sup> and muscle<sup>14</sup> have been studied by this process, where the optical imaging modalities have included brightfield, OCT, and second harmonic generation (SHG). In many cases, the increase in penetration depth was  $\sim 100$  to 300%. It is a widely accepted mechanism that a reduction in the reduced scattering coefficient,  $\mu'_s$ , is responsible for this effect, where the optical clearing potential has been defined as  $(\mu'_s \text{ cleared} / \mu'_s \text{ uncleared})$ .<sup>8</sup> As described by Mie theory, this ratio becomes infinite for the case of perfect index matching.<sup>15</sup> However, the exact nature of the index matching

Address all correspondence to Paul J. Campagnola, Univ. of Connecticut Health Center, Center for Cell Analysis and Modeling, Dept. of Cell Biology, Farmington, CT 06030; Tel: 860 679 4354; Fax: 860 679 1039; E-mail: campagno@neuron.uchc.edu

process, i.e., the specifics of the reagent-tissue interactions, has not been uniquely identified in all cases. Additionally, while some studies have examined the physiological and structural similarities before and after clearing,<sup>16,17</sup> additional research is required to establish the clearing method as a clinical diagnostic tool.

Our previous work in this area employed optical clearing together with SHG microscopy to obtain greater imaging depth in muscle tissue, where we demonstrated that treatment with 50% glycerol increased this depth by  $\sim 2.5$ -fold.<sup>14</sup> Through Fourier and wavelet transforms, we also demonstrated that clearing did not appreciably disrupt the contractile apparatus, i.e., the sarcomere lengths were unchanged. Additionally, polarization anisotropy measurements relating to the collagen helical assembly revealed no differences following clearing. Through our experimental evidence, we suggested a mechanism based on reduction of the secondary inner filter, i.e., absorption of the forward-directed SHG wave, to account for the observed increase in penetration depth. A similar effect was also recently observed by Rothstein et al.<sup>18</sup> in mouse skeletal muscle *in vivo*, where significant absorption of NADH autofluorescence was seen in this same wavelength range.

Given the potential impact of optical clearing, we have expanded our experimental work to include modeling efforts to further establish the capabilities and provide definitive mechanisms for the clearing process in both muscle and collagenous tissues. SHG is ideally suited for this task, due to its three-dimensional (3-D) imaging abilities as well as its exquisite sensitivity to changes in tissue assembly. Additionally, SHG imaging has great applicability in terms of endogenous tissue imaging,<sup>19-24</sup> and this potential may be further improved through the use of optical clearing. Thus, it is important to understand the clearing mechanism and elucidate any limitations in the technique in different tissue types. For example, cellular tissues such as muscle may respond differently to clearing than purely extracellular matrix (ECM) tissues. In this paper, we present methods to quantitatively determine the SHG 3-D image enhancement in collagenous ECM and muscle tissues as well as provide further insight into the clearing mechanisms.

Our approach is to measure the axial dependences of the forward-directed SHG and the ratio of the forward/backward intensities over a range of glycerol concentrations. These 3-D data relate to SHG creation attributes (intensity and directionality) as well as the subsequent propagation losses due to multiple scattering and absorption. This approach, coupled with corresponding Monte Carlo simulations of the photon propagation based on measured bulk optical parameters (scattering coefficient  $\mu_s$ , scattering anisotropy  $g$ , and refractive index at the fundamental and SHG wavelengths before and after clearing), will provide a definitive analysis of the contributions of the primary and secondary filters on the image intensities. Through these studies, we show that reduction of the primary filter following clearing dominates the observed axial attenuation response in both muscle and tendon. We suggest that the mechanism in muscle arises from matching the refractive index of the muscle cells with the higher index of the surrounding perimysium, where the measured decrease in  $\mu_s$  is in good agreement with that predicted by Mie theory. Additionally, we also find that the integrated 3-D SHG inten-

sity in collagenous tendon increases with clearing, where the experimental data is in good agreement with simulations based on the measured decrease in  $\mu_s$ .

## 2 Experimental Methods

### 2.1 Tissue Preparation

The muscle samples were obtained from adult CD1 mice. The mice were anesthetized by CO<sub>2</sub> narcosis, sacrificed, and the lower limbs dissected. Snips of quadriceps femoris or gastrocnemius muscles were dissected by a 4.0-mm outer diameter  $\times$  80-mm skeletal muscle biopsy needle and then sliced with a vibratome to thicknesses of 100 to 400  $\mu\text{m}$ . These were briefly washed in PBS buffer and then immersed into clearing media. The clearing solutions contained 25, 50, or 75% glycerol, 70 mM NaCl, 1 mM KCl, 1.5 mM MgCl<sub>2</sub>, 10 mM imidazole-HCl pH 7.0, 5 mM EGTA, and 1 mM PMSF. Tail tendon was dissected from adult Sprague-Dawley rats and adult CD1 mice. Rat tails were used for measurement of the bulk optical properties, as those from mice were not sufficiently large to cover the apertures of the integrating spheres. In each case, to isolate tendon fibrils, the skin was pulled from the tail, and strips of tendon collagen were carefully detached from the bones. The tendon was carefully unwrapped for integrating sphere measurements. This technique was deemed essential, as entire tendon is too thick to permit full light penetration. SHG analysis of unwrapped tendon revealed little damage to the fibrillar structure, but the process did lead to the introduction of relatively large voids, which were sporadically spaced. Thus, a best effort was made to perform measurements on uniform locations (greater than the spot size of the laser beam). It was then immersed in the same clearing solutions as muscle. Mouse tendon was used for SHG imaging, as whole rat tendons were too thick to permit imaging in the forward direction. Before imaging, the tendon was cut into smaller fragments (1 cm long), positioned on the microscope slide, immersed in the clearing solution, and secured under a silicone grease-mounted coverslip.

### 2.2 SHG Microscope

The SHG imaging system consists of a laser scanning head (Olympus Fluoview 300) mounted on upright microscope (Olympus BX61) and coupled to a mode-locked Titanium Sapphire laser. All measurements were performed with a laser fundamental wavelength of 890 nm with average power of  $\sim 5$  to 20 mW at the specimen. The microscope simultaneously collects both the forward and backward components of the SHG intensity. In the former, a long working distance  $40 \times 0.8$  N.A. water-immersion objective and a 0.9 N.A. condenser provide excitation and signal collection, respectively. The backward component is collected through the excitation objective in a non-descanned configuration. In each channel, the SHG signal is isolated with a dichroic mirror and 10-nm bandpass filter (445 nm, Semrock). The signals are detected by two identical photon-counting photomultiplier modules (Hamamatsu 7421). The SHG wavelength (445 nm) was confirmed with a fiber optic spectrometer (Ocean Optics). There is no detectable autofluorescence for either collagen or muscle at this excitation wavelength.

**Table 1** Bulk optical parameters for striated muscle at the fundamental and SHG wavelengths.

$\lambda$	457 nm				890 nm			
% Glycerol	Control	25%	50%	75%	Control	25%	50%	75%
$g$	0.96	0.96	0.96	0.96	0.96	0.96	0.96	0.96
$\mu_s$ (cm <sup>-1</sup> )	506±225	229±71	71±25	28±2.4	285±113	138±45	29±5	26±6
$\mu_a$ (cm <sup>-1</sup> )	9.1±3.1	8.8±1.4	3.8±1.5	3.3±1.2	5.9±1.5	2.9±0.5	1.9±0.5	1.4±0.2

### 2.3 Image Analysis

SHG image stacks were quantitatively analyzed with ImageJ software (<http://rsb.info.nih.gov/ij/>). A coumarin dye slide emitting two-photon excited fluorescence at the SHG wavelength (~450 nm) was used to calibrate both signal collection channels to account for uneven losses in optical paths and relative collection efficiency of the two detectors. Since the forward-to-backward (F/B) fluorescence ratio from a dye slide is assumed to be one, it becomes the normalization factor for the two collection geometries.

### 2.4 Bulk Optical Parameters

The Monte Carlo simulations (see the following) require the following bulk optical parameters: scattering coefficient ( $\mu_s$ ), absorption coefficient ( $\mu_a$ ), and anisotropy ( $g$ ) of the tissue at the fundamental and SHG wavelengths. We determined these parameters for muscle and tendon at 457 nm (Ar<sup>+</sup> line approximating the SHG wavelength) and 890 nm (unfocused Ti:Sapphire) using the following measurements. The diffuse reflected and transmitted intensities were measured by placing the specimen (~100  $\mu$ m in thickness) between a dual integrating sphere setup, where the entrance and exit spheres have 3 and 2 ports, respectively. In order to avoid multiple interfaces, tissues were mounted on custom-built holders for unobstructed positioning between the spheres and kept hydrated during the measurement. The refractive indices necessary for the extraction of the scattering and absorption coefficients<sup>25</sup> were determined using the method of Li and Xie,<sup>26</sup> where the specimen is placed on a cylindrical lens and the critical angle for total internal reflection is measured. Utilizing the measured transmittance and reflectance, anisotropy factor ( $g$  assumed to be 0.96),<sup>27</sup> the index of refraction and the tissue thickness, inverse Monte Carlo simulations are utilized to determine the absorption coefficient  $\mu_a$ , and scattering coefficient  $\mu_s$ , which is related to the scattering coefficient  $\mu'_s$  by:

$$\mu'_s = \mu_s(1 - g). \quad (1)$$

### 2.5 Monte Carlo Simulations

For comparison with the experimental 3-D data and to decouple the respective roles of the primary and secondary inner filter effects on SHG creation and propagation, Monte Carlo simulations based on photon diffusion using the bulk optical parameters were performed. To this end, we adapted a previous model by Wang et al.<sup>28</sup> to calculate the escape probabilities for the forward and backward channels. The simulation requires the bulk optical parameters determined in Sec. 2.4

and tissue thicknesses. Optical sectioning is simulated by calculating the fraction of incident laser photons that arrive at the focal point at a given depth based on the 0.8 NA in conjunction with the measured value of  $\mu_s$  at 890 nm. This simulation results in the determination of the primary filter effect on the SHG intensity (proportional to the square of the 890 transmission) at all depths in the tissue. Secondary filter effects are then modeled by calculating the propagation losses governed by the bulk optical properties at the SHG wavelength.

## 3 Results

### 3.1 Mechanism of Optical Clearing in Muscle Tissue

In our previous work, we postulated that the increase in SHG imaging depth in striated muscle arose from a reduction in the secondary inner effect, i.e., reduced absorption of the SHG as it forward-propagated through the remainder of the tissue. We now enhance this preliminary effort through knowledge of the bulk optical parameters and use of Monte Carlo simulations to unambiguously determine the optical clearing mechanisms. The results from the integrating sphere measurements for the scattering coefficient ( $\mu_s$ ) and absorption coefficient ( $\mu_a$ ) for the control and for glycerol concentrations of 25%, 50%, and 75% at 457 nm (SHG) and 890 nm (fundamental) are summarized in Table 1. We assumed an anisotropy value of  $g = 0.96$  from the literature,<sup>27</sup> as we were unable to cut sufficiently thin sections to ensure an accurate measurement, where these would have needed to be ~20  $\mu$ m (~1/ $\mu_s$ ) to avoid convolution effects from multiple scattering. We first noted that at both wavelengths,  $\mu_s \gg \mu_a$ . We further observed that treatment with glycerol greatly reduces the scattering coefficients at both wavelengths, where the effect is highly pronounced for the 50% and 75% cases, and is approximately an order of magnitude relative to the control. However, a corresponding reduction occurs with 25% glycerol application as well. The absorption coefficients also decrease with clearing, presumably due to loss of cytoplasmic proteins; however, the initial magnitudes were much smaller than those of  $\mu_s$ . We note that these bulk optical parameters are not obtainable from the 3-D image data directly, as the depth-dependent SHG intensity is linked directly to the square of laser intensity (and thus conversion efficiency), emission directionality, and subsequent propagation losses.

To gain further insight into the clearing mechanism, we measure the axial attenuation of the forward SHG signal as a function of glycerol concentration. This response is resultant from the combination of the primary and secondary filter effects on the SHG creation and propagation, respectively. Rep-

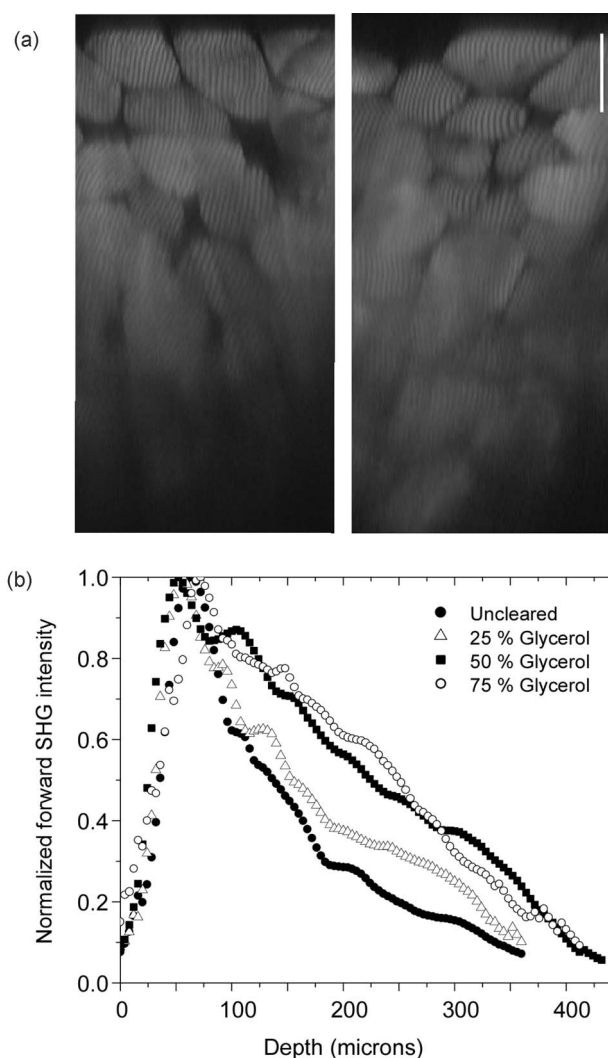


**Fig. 1** 3-D SHG imaging of cleared striated muscle tissue. (a)  $x$ - $z$  projections of the SHG image stacks for 25% (left) and 75% (right) glycerol treatments. Scale=50  $\mu\text{m}$ . (b) The normalized axial attenuation of the forward SHG intensity for the control and three glycerol treatments. All the glycerol treatments result in greater imaging depth relative to the control.

representative  $x$ - $z$  projections used for this analysis for the 25% and 75% glycerol are shown in the top panels in Fig. 1(a). The attenuation curves,  $I_{SHG}(z)$  versus  $z$  are calculated as the average of 15 to 20 image stacks, and the resulting data for the control and three glycerol concentrations are shown in Fig. 1(b). The data are normalized to the maximum in each image stack for each percent glycerol treatment, and the averages of these fractional glycerol treatments are then normalized to each other. Application of glycerol results in a swelling of the muscle cells, where the higher concentrations result in thicker tissues for the same exposure time. Thus, it is necessary to consider swelling in addition to bulk optical parameter changes when directly comparing the data because the physical thickness affects the subsequent measured signal attenuation and directionality. Due to decreased scattering and absorption losses, we observed that the 50% and 75% glycerol treatments result in similar axial attenuation profiles, showing

reduced attenuation relative to the 25% case and control. These trends are indicative of the corresponding reduction in the measured  $\mu_s$  values associated with optical clearing.

These measured attenuation curves [Fig. 1(b)] cannot be represented as single exponentials, as they arise from both the primary filter effect on the laser intensity as well as the secondary filter processes directly affecting the SHG intensity. Moreover, the relative contributions of these factors are depth-dependent. Thus, to decouple the individual filter effect, we perform Monte Carlo simulations of the depth-dependent relative SHG generation and propagation using the bulk optical parameters (Table 1), comparing our final simulated SHG transmittance to the experimental data. In these simulations, we assume a fixed SHG scattering cross-sectional area, 100% forward emission directionality (see the following justification), and 100% conversion efficiency for primary photons contained within this focal volume at the prescribed penetration depth.

Figure 2(a) shows the square of the transmission of the laser through 200  $\mu\text{m}$  of propagation, representing the primary filter effect alone on the resulting laser intensity and thus the relative intensity of the created SHG throughout the axial profile. The simulated curves strongly resemble the SHG attenuation data [Fig. 1(b)] in two important ways: First, the simulations show the similarity of the 50% and 75% glycerol cases, as well as the inbetween behavior of 25% treatment with respect to the uncleared tissue. Second, these curves also reproduce the overall curvature of the experimentally observed data, where the highly cleared tissues are more monotonic in the intensity attenuation, and the uncleared tissue and 25% cases have an inflection point in the middle of the depth response. We note that for each treatment, the rate of attenuation predicted by the simulation is more rapid than for the analogous experiment. While this could possibly arise from inaccuracies in measurement of the bulk optical parameters (dominated by  $\mu_s$  values), we will describe in Sec. 4 that the disagreement between the experiments and simulations is largely due to differences in SHG conversion efficiencies in the treated tissues. However, for the current context, we note that these determinations were made self-consistently, and we use the resulting values in a comparative analysis between the cleared and uncleared tissues.

This exercise leads to the unintuitive conclusion that the axial attenuation response is largely determined by the primary filter effect, rather than losses due to the secondary filter effects of scattering and absorption of the SHG signal. To further illustrate this comparison, the simulated SHG attenuation curves (governed by both the primary and the secondary filters) in Fig. 2(b) are shown to track the attenuation of the square of the laser transmittance plotted in Fig. 2(a). Thus, while  $\mu_s$  for the uncleared tissue at 890 nm ( $285\text{ cm}^{-1}$ ) is approximately half the 457-nm value, it is still significant in the present case, where the 35- $\mu\text{m}$  mean free path (MFP;  $1/285\text{ cm}^{-1}$ ) is much less than the thickness of the tissue. Additionally, the primary filter has a quadratic effect on the SHG conversion efficiency and thus dominates the subsequent propagation losses of the second harmonic signal through the turbid media.

To further demonstrate the impact of the reduction of  $\mu_s$ , we can also compare the experimental and simulated axial

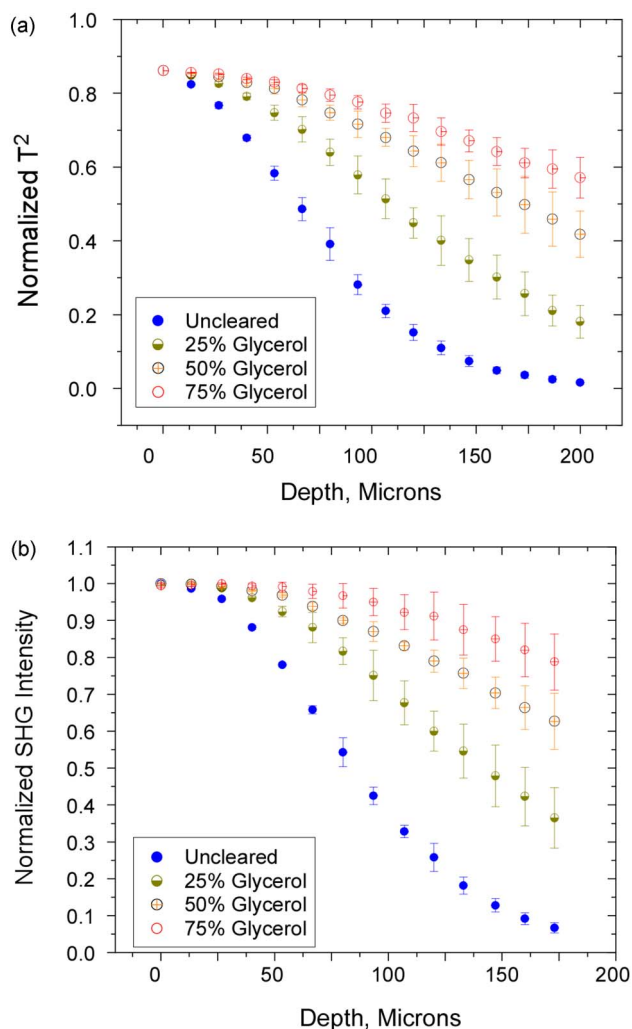


**Fig. 2** Monte Carlo simulations of the SHG attenuation curves for the experimental cases shown in Fig. 1 using the bulk optical parameters tabulated in Table 1. Simulations of the axial dependence of the primary filter effect by calculation of the square of the transmission ( $T^2$ ) at 890 nm. (b) Simulation of the axial dependence of the SHG intensity arising from both primary and secondary filter effects. Comparison of these simulations with the experimental data indicates that the axial SHG response is dominated by the primary filter effect on the laser intensity.

dependence of the ratio of the F/B detected SHG intensity for cleared and uncleared tissues. This response is governed by the SHG creation directionality as well as the bulk optical parameters at the SHG wavelength. The detected backward SHG is a superposition of direct quasi-coherent emission<sup>29</sup> and a multiple scattered incoherent component. In general in turbid tissue specimens, the measured signal results from both contributions,<sup>30</sup> where the relative magnitudes depend on the morphology of the tissue assembly as well as the bulk optical parameters. Previously, we assigned the myofibril as the SHG producing element,<sup>31</sup> and based on our recent theoretical analysis,<sup>29</sup> the SHG creation in muscle should be essentially all forward directed. Thus, the depth dependence of the F/B ratio in muscle tissue will be governed by  $\mu_s$  and  $g$  at  $\lambda_{SHG}$ .

Monte Carlo simulations of F/B versus  $z$  for the control

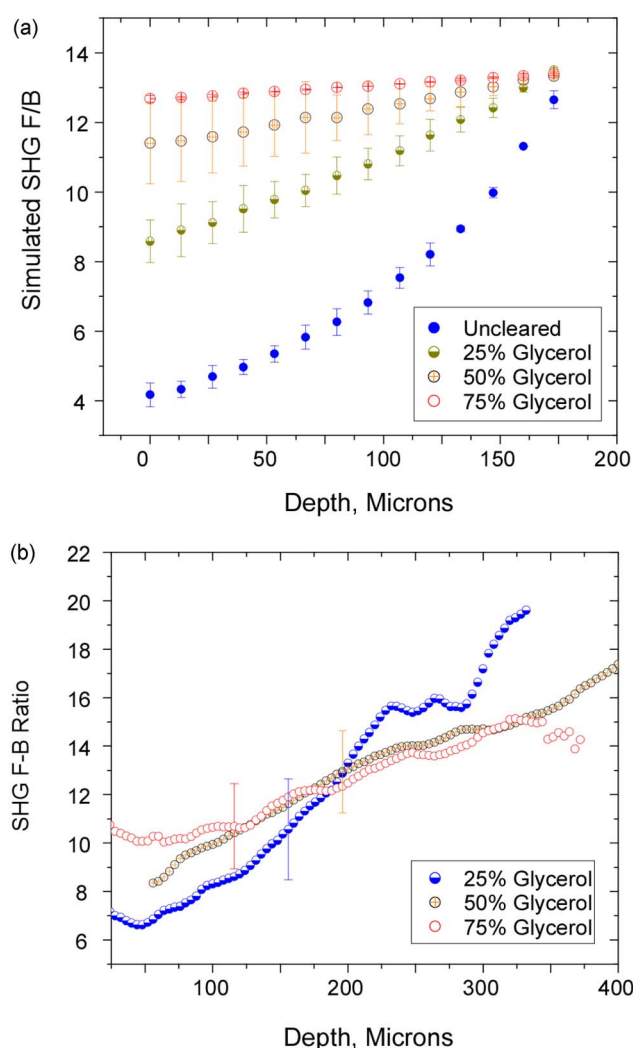


**Fig. 3** Comparison of the axial dependence of the directionality of the SHG propagation for the control and three glycerol treatments. (a) Monte Carlo simulations of the depth-dependent forward-to-backward (F/B) ratio, assuming 100% forward creation directionality; and (b) experimental F/B data. The agreement between the experimental and simulation of the initial ratio indicate that the SHG creation directionality is 100% forward. The data for the experimental control was in the noise floor, and a meaningful F/B ratio could not be ascertained.

and tissues cleared with three different glycerol concentrations (25%, 50%, and 75%) are shown in Fig. 3(a). These simulations show that for all the tissues, the F/B increases with increasing depth into the muscle tissue and further that the overall F/B level increases with glycerol concentration (which acts to decrease the number of scattering events, thus reducing the backward signal, which predominantly arises from multiple scattering events). As also shown in Fig. 3(a), the curves merge at the back side of the tissue. This result is a consequence of photon diffusion theory, where at least one MFP is required between the location of the emitted photon to the forward boundary of the specimen for efficient multiple scattering to occur.<sup>28</sup> Thus at increasing focal depths, the probability of scattering collisions is decreased as the remaining thickness becomes much shorter than the MFP, which

becomes longer for the cleared tissues. The corresponding experimental data for the 25, 50, and 75% glycerol treated muscle are shown in Fig. 3(b). We observe that the F/B at the top of the stack increases with glycerol concentration, where these values range from 7 to 10 and increase to  $\sim 15$  at the bottom tissue exit. Thus, the experimental data qualitatively match the trends predicted by the Monte Carlo simulations assuming 100% forward SHG creation. This rise of the F/B with increasing depth delineates the effect of the secondary filters on the measured SHG signal, where these diminish with the decrease in exit path length. Based on the measured bulk optical parameters, where  $\mu_s > \mu_a$ , we assign the propagation losses in all cases primarily to multiple scattering as opposed to absorption.

We note that we performed this measurement for uncleared tissue as well; however, the detected backward signal was in the noise floor for much of the depth profile, and we could not extract a meaningful F/B plot. Further confounding this measurement was the overall reduced SHG intensity relative to the cleared cases deep into the tissue [see Fig. 1(b)]. We attribute this effect to the large scattering coefficient at 457 nm ( $\mu_s \sim 500 \text{ cm}^{-1}$  or MFP  $\sim 20 \mu\text{m}$ ) in conjunction with the limited collection aperture. Thus, deep into the tissue, a fraction of the multiple scattered photons are scattered into a radius at the exit of the tissue larger than the first element of the excitation objective lens ( $r \sim 1 \text{ mm}$ ), resulting in missed photons. Similarly, we attribute the crossing of the 25% curve over both the 50% and 75% in the experimental curve at deeper depths to incomplete collection of all the backscattered photons, resulting in an artificially high F/B. The tissues cleared with higher glycerol concentrations do not suffer from this effect, as their associated photon trajectories are more on-axis.

Good agreement between the experimental and theoretical F/B data (approximately 10:1) at the top of the 3-D image stacks is attributed to the validity of our theoretical assumption that SHG creation is essentially forward, which also has been found in other experimental observations.<sup>32</sup> This emission directionality is a physically interpretable result, as the myofibril (i.e., the SHG-producing elements) diameters are on the order of a micron, and based on theoretical predictions,<sup>24,29</sup> SHG-creating structures on this size scale or larger than  $\lambda_{SHG}$  result in near 100% forward emission. By contrast, if appreciable initial backward emission occurred, a smaller F/B would be observed experimentally at all depths until the exit of the tissue.<sup>30</sup>

### 3.2 Optical Clearing in Tendon

As SHG imaging of collagenous tissues in conjunction with optical clearing has great potential, the combined use of these techniques warrants further investigation. Here, we explore the mechanism and capabilities of optical clearing in 3-D imaging of tendon by making quantitative assessments of the imaging depths and intensities and subsequent modeling of these effects by Monte Carlo simulation of the SHG creation and propagation. Tendon is an ideal candidate for these studies due to the highly regular fibril structure as well as its homogeneous composition.

Figure 4(a) shows  $x$ - $z$  projections of 50% glycerol treated mouse-tail tendon immediately (left) and then 5 h (right) after

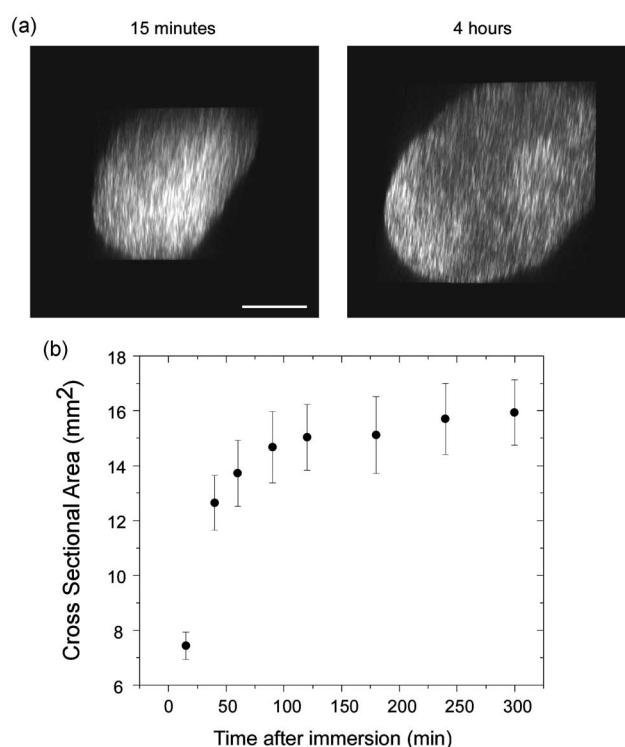


**Fig. 4** 3-D SHG imaging of 50% glycerol treated tendon. (a)  $x$ - $z$  projections of the SHG image stacks for 15 min (left) and 5 h (right) after immersion. Scale =  $50 \mu\text{m}$ . Significant swelling is observed. (b) Resulting cross-sectional area over a 5-h time course. The area increases by approximately twofold.

immersion. We note that while these cross sections are similar in appearance in terms of the collagen assembly, the cleared tissue exhibits significant swelling. The cross-sectional area of the tendon over 5 h of immersion is plotted in Fig. 4(b), showing an approximately 2.2-fold increase. We note that while the increase in the fibril spacing is below resolution of the microscope, it is manifested in decreased intensity in single optical sections due to a decrease in the local concentration of “harmonophores.”

As the tissue remains intact and does not appear damaged following this expansion, an interesting question then regards the effect of clearing on the overall SHG intensity. We measured the resulting intensity through an entire cross section over a 5-h time course, and the results are shown in Fig. 5, where a  $\sim 2$ -fold enhancement in the integrated SHG intensity is observed. We stress that this increase in SHG intensity occurs over the volume of the swelled tissue, where, by contrast, the intensities in individual optical sections are lower. We believe that the overall increase in integrated volumetric SHG intensity is indicative of the retention of morphological structure through the clearing process, although swelling is present. Moreover, the clearing process was reversible upon washing out the glycerol with PBS, furthering our conclusion that the tissue structure was not detrimentally altered. This point is illustrated in Fig. 6, showing the 3-D rendered image stacks from precleared (a), cleared (b), and reversed (c) tendon.

To interpret these data, we measured the bulk optical parameters for control and 50% glycerol treated tendon at the

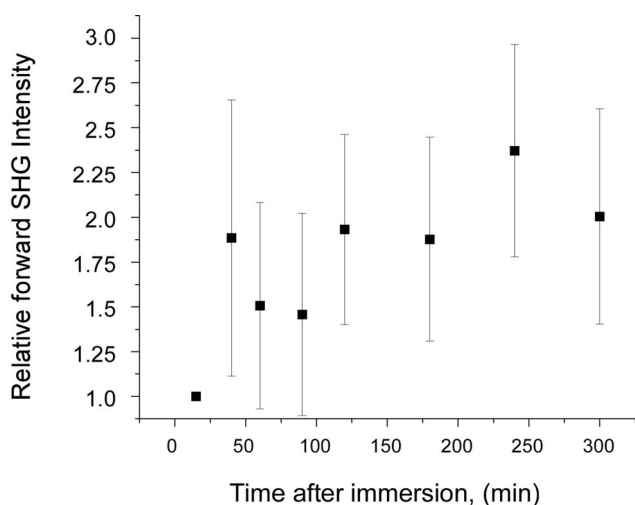


**Fig. 5** 3-D integrated SHG intensity for the time course shown in Fig 4. The overall SHG increases by twofold, despite the lower intensity in single optical sections.

fundamental and SHG wavelengths, and the results are shown in Table 2. We observe that the scattering coefficients drop dramatically, e.g., almost 20-fold at  $\lambda_{SHG}$  upon clearing. This presumably arises from replacing interfibril water with the index-matching glycerol, where this results in increasing the interfibril spacing as well.

This reduction of scattering is also reflected in the SHG forward attenuation data. Figure 7 shows this data for the control and 25, 50, and 75% glycerol treated tendon, where the tissues were cleared for 12 h. The imaging depth in each case represents the physical thickness of the tendons before and after clearing. As in the case of muscle, the rates of attenuation are much slower with respect to depth for the increasingly cleared tissues. For example, the 75% treatment is the most dramatic case and exhibits a nearly flat response over  $\sim 200 \mu\text{m}$  of depth into the tissue.

To determine whether the integrated increase in SHG intensity (Fig. 5) is consistent with reduction in  $\mu_s$ , we performed analogous Monte Carlo simulations of the SHG forward attenuation as was done for the muscle tissue. Here, we perform the comparison at 5 h post-immersion. The experimental data and simulations for the control and 50% are shown in Figs. 8(a) and 8(b), respectively, and the trends are in qualitative agreement. Namely, the SHG for the uncleared tissue experiences a rapid attenuation through  $100 \mu\text{m}$  in

**Table 2** Bulk optical parameters for tendon at the fundamental and SHG wavelengths.

$\lambda$	457 nm		890 nm	
	Control	50%	Control	50%
% Glycerol	Control	50%	Control	50%
$g$	0.96	0.96	0.96	0.96
$\mu_s$ ( $\text{cm}^{-1}$ )	$510 \pm 300$	$27 \pm 7.1$	$399 \pm 44$	$3.1 \pm 2.1$
$\mu_a$ ( $\text{cm}^{-1}$ )	$5.0 \pm 1.7$	$2.1 \pm 1.1$	$2.2 \pm 0.3$	$1.5 \pm 0.7$

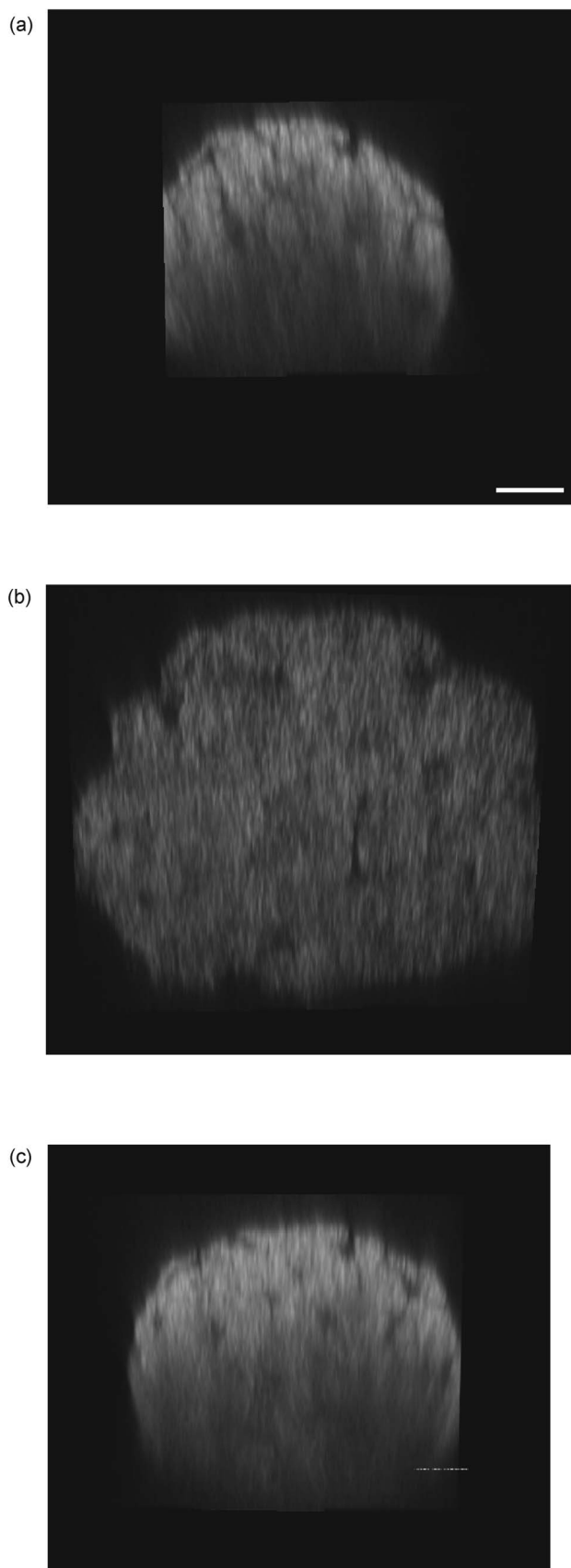


**Fig. 6** The clearing in tendon with 50% glycerol is reversible. The 3-D renderings are for the SHG of (a) uncleared tendon, (b) cleared tendon, and (c) tendon following washing in PBS. Scale bar =  $20 \mu\text{m}$ .

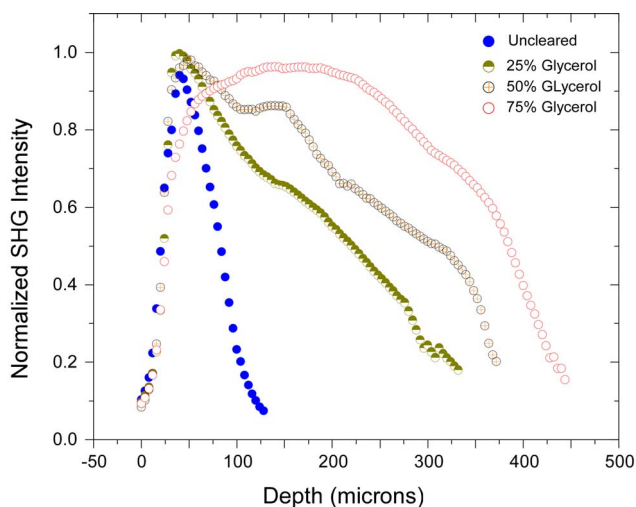


**Fig. 7** The normalized axial attenuation of the forward SHG intensity for the control and three glycerol treatments for tendon after 12 h of immersion. Increasing the glycerol fraction results in increased swelling as well as a decrease in the rate of the axial attenuation.

both the experimental data and the simulation. The experimental and simulation results for the 50% case are similar, where the SHG intensity decreases are approximately 20% and 5%, respectively. This difference in the experiment and the simulation probably arises from the large variability in measuring absolute values of the scattering coefficient variations in the sample preparation, which involves unrolling the tendon fibrils, as was required for experimental compatibility. However, we use these  $\mu_s$  values only for comparative analysis, and the fact that the trends in the data and modeling are similar indicates greatly reduced scattering in the cleared tissue relative to the control. As a further comparison, we can estimate the overall enhancement of the SHG throughout the 3-D volume by integrating the areas under the curves. This analysis results in an overall intensity increase of factors of 2.2 and 3 for the experiments and simulations, respectively, and thus is in qualitative agreement. Therefore, 3-D imaging and modeling allows us to conclude that optical clearing in tendon does indeed increase the SHG intensity to the extent predicted by the reduction of scattering.

#### 4 Discussion

To make quantitative assessments of the clearing process in terms of the mechanism and capabilities for image enhancement, we used the combined approach of 3-D SHG imaging and Monte Carlo simulations of the photon propagation based on the measured bulk optical properties as a function of glycerol concentration. This approach allows decoupling of the primary and secondary filter effects on the SHG intensities and elucidated physical mechanisms behind optical clearing of muscle and tendon.

Inspection of the bulk optical parameters in Table 1 now shows unambiguously that glycerol treatment reduces the scattering coefficient of striated muscle by more than an order of magnitude at both the fundamental and the SHG wavelengths. Comparison of the measured axial attenuation [Fig. 1(b)] with Monte Carlo simulations based on these optical

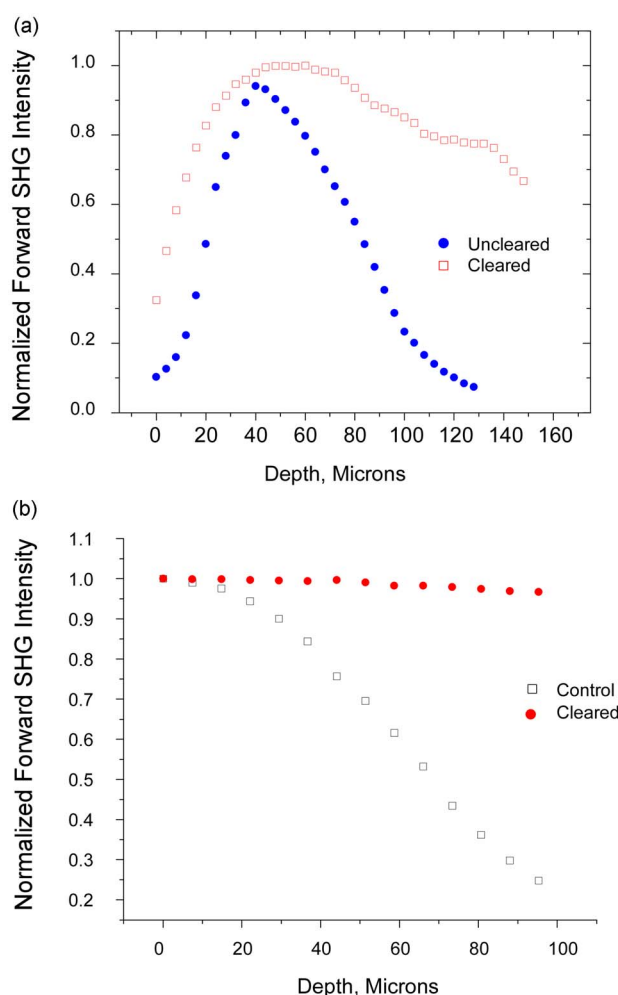


**Fig. 8** Comparison of the experimental (a) and simulated (b) axial response of tendon before and after 50% glycerol treatment 5 h post-immersion. Integration under the curves reflects the entire SHG intensity before and after clearing, where the experiment and simulations show overall SHG enhancement factors of two- and three-fold, respectively. These results indicate that the measured increase in SHG is consistent with the decrease in scattering measured with integrating spheres.

parameters allows the isolation of the primary [Fig. 2(a)] and secondary filter effects [Fig. 2(b)] on the 3-D response. Examination of these simulations allows us to conclude that the measured axial response is largely set by the primary filter effect on the SHG creation efficiency, i.e., scattering losses of the laser dominate the secondary losses due to the quadratic power dependence on the SHG conversion. We note that as shown by Huxley and Hanson,<sup>33,34</sup> glycerol treatment will reduce the intracellular optical density by leakage of cytoplasmic proteins by a small fraction,  $\sim 10$  to 15%. However, the absorption coefficients at 457 nm (see Table 1) even before clearing are small in comparison to the scattering coefficients and contribute little to the SHG attenuation profile.

Thus, we need to consider the changes in cellular properties that result in the significant reduction of scattering. While the bulk of striated muscle tissue consists of acto-myosin complexes, each muscle cell is wrapped by perimysium, which is a thin layer ( $\sim 2 \mu\text{m}$ ) of collagen. While this layer

does not significantly contribute to the overall thickness of the tissue, it does create a refractive index mismatched interfacial boundary between the cells, where the refractive indices of collagen in tissue and muscle are 1.47 and 1.38, respectively. The effect of the mismatch on the scattering coefficient can be examined in the context of Mie theory. As described by Tuchin<sup>15</sup> for a monodisperse model of dielectric spheres, the reduced scattering coefficient is given by:

$$\mu'_s = 3.28\pi a^2 \rho_s \left(\frac{2\pi a}{\lambda}\right)^{0.37} (m-1)^{2.09}, \quad (2)$$

where  $a$  is the sphere radius,  $\rho$  is the sphere volume density, and  $m=n_s/n_0$  is the ratio of the refractive index between the scattering particle and background. This relation predicts that  $\mu'_s$  is a steep function of the magnitude of this mismatch and approaches zero for the perfectly matched case.

While this relation applies rigorously for dielectric spheres, we can use it in an analogous manner to describe the role of refractive index matching between the muscle cytoplasm and surrounding perimysium in decreasing the reduced scattering coefficient. Treatment with glycerol ( $n=1.47$ ) permeabilizes the cell membrane and exchanges with the water in the cell, thereby increasing the intracellular refractive index, and thus decreasing the mismatch with the higher-index perimysium. For example, assuming an initial index for muscle of 1.38 and using the weighted average law of Gladstone and Dale, we calculate the effective intracellular refractive indices for 25, 50, and 75% glycerol treatments to be 1.40, 1.43, and 1.45, respectively. We then use these values in conjunction with the index-matching term in Eq. (2) [ $(m-1)^{2.09}$ ], where we associate the perimysium ( $n=1.47$ ) and muscle cells as the scattering objects and background, respectively. This then predicts that the scattering coefficient at the  $\lambda_{SHG}$  after 75%, 50%, and 25% glycerol treatment should decrease by factors of  $\sim 25$ -, 6-, and 2-fold, respectively. The resulting values are in good agreement with the measured parameters shown in Table 1, where the corresponding factors were 18, 7, and 2, respectively. By this argument, higher glycerol concentrations should lead to increased imaging depths due to the decreased mismatch and concurrent reduction in scattering. This is borne out by the attenuation data in Fig. 1(b), which shows the normalized SHG intensity through the tissues, where higher glycerol concentrations do indeed lead to greater imaging depths as well as decreased rates of attenuation.

Given the agreement of measured and predicted values of  $\mu'_s$ , we must consider that any underlying factors that would systematically cause the qualitative and quantitative disagreement between the experimental and simulated attenuation data in Figs. 1(b) and 2, respectively, are all normalized to each maxima to allow comparisons to each other. These attenuation curves result from the bulk optical parameters at the fundamental and SHG wavelengths (primary and secondary filters, respectively), the initial emission directionality, and the relative SHG conversion efficiency of each tissue. In our recent work on the oim disease model,<sup>35</sup> we discussed how tissues of lower conversion efficiency would result in a faster attenuation with respect to depth. This is analogous to the concept of “weighted photons” introduced by Welch and co-workers for

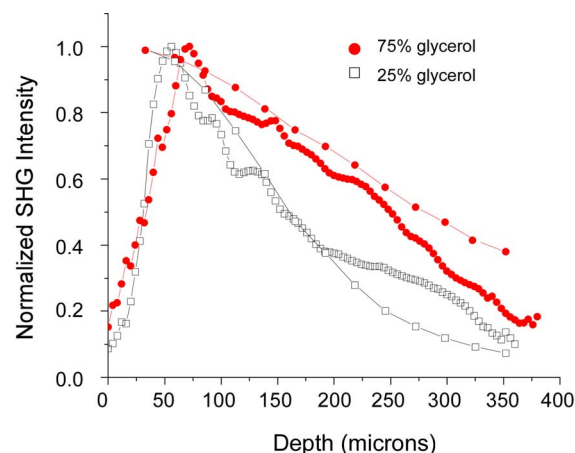


**Fig. 9** Comparison of the simulations and experimental data for the 75% and 25% glycerol treatment, considering a relative efficiency of twofold greater for the former treatment.

making comparisons between the attenuation of fluorescent photons emitted from fluorophores with different absorption coefficients and quantum yields.<sup>36</sup>

We can use this concept to explain the difference between the experiments and the simulations. The simulations in Fig. 2 assumed 100% conversion efficiency of the laser photons that arrive in the focal volume for each tissue. However, the conversion efficiency between the cleared and uncleared tissues will not be the same. Namely, as we previously reported,<sup>14</sup> the tissue swells from  $\sim 50$  to 100%, and the SHG from a given focal plane from the cleared tissues is weaker than the control. However, integration of the intensity throughout the volume yielded approximately constant intensity. As shown in Fig. 9, the simulations for the cases of 25% and 75% glycerol reproduce the experimental results qualitatively and almost quantitatively if we assume a twofold higher conversion efficiency for the former (the control and 50% are omitted for clarity of presentation).

We can explain the physical basis of different conversion efficiencies in the cleared and uncleared tissues using phase matching arguments. Recently, we introduced the concept of “domains” to describe the SHG creation attributes of emission directionality and conversion efficiency in fibrillar tissues.<sup>29</sup> Here, a domain can be a large fibril or an assembly of smaller fibrils packed closely together. Within the coherence length (maximum of a few  $\mu\text{m}$  limited by dispersion), the SHG will build up in a domain or closely spaced domains (in the axial direction). In the case of striated muscle, the harmonophore is the myofibrils, which are approximately 1 to 2  $\mu\text{m}$  in diameter and stacked together to form bundles. For the case of clearing, the tissue swells (50 to 100%), and the myofibril spacing concurrently increases. This reduces the SHG buildup (and thus conversion efficiencies), and the myofibrils no longer coherently interact as efficiently to contribute to the SHG intensity. Based on our published calculations, a decrease in domain size of two fold would also have approximately a twofold reduction of SHG buildup.<sup>29</sup> This reduction in domain size would occur for the case of 100% increase in the tissue diameter.

While the index-matching considerations in collagenous tendon are simpler due to the homogeneity of the tissue, it is important to unambiguously determine the effect of clearing on SHG imaging and further determine whether there are associated detrimental effects arising from this process. For example, Yeh et al. previously showed that glycerol led to decreased SHG in skin and skin models, although the transparency was visually increased.<sup>37</sup> Previously, we also reported a similar loss of SHG intensity in tendon, by comparing the integrated intensity in single optical sections.<sup>14</sup> Similarly, Yeh and Hirshburg have suggested that clearing agents reversibly affected the higher-order collagen structures.<sup>16</sup> Reconsidering this issue with 3-D SHG quantitative measurements and modeling has led us to a different conclusion. After 12-h immersion in glycerol, a  $\sim 3$ -fold swelling of the tendon occurred; however, no disruption in the fibril assembly, i.e., shortened or broken fibrils, was seen, either in the forward or backward channels, where the latter is highly sensitive to the extent of packing.<sup>29</sup> Integration of the 3-D SHG signal throughout the entire cross section yields an *increase* in the intensity (2 to 3-fold), although individual optical sections are indeed dimmer, as previously reported. Using Monte Carlo simulations, we tested whether this increase was consistent with the reduced scattering coefficients following clearing (see Table 2). The simulations also showed an increase in overall SHG intensity in this same range. We ascribe the reduction of scattering (see Table 2) to both index matching by replacement of interfibril fluid with glycerol, and to the concurrent swelling that increases the distance between the fibril scatterers. We suggest this reversible increase in interfibril distance may be analogous to the dissociation previously reported in skin and RAFT models.<sup>37</sup>

Thus, optical clearing appears to be useful in enhancement of SHG imaging of collagen in terms of increasing achievable imaging depths. This capability should be enabling for performing polarization measurements in collagenous tissues to determine detailed structural information. This analysis can be important in assessing differences in normal and diseased tissue but may not always be possible due to loss of the laser polarization. For example, while they did not attribute the cause to scattering, Stoller et al.<sup>38</sup> showed that the angular dependence of the laser polarization with respect to the fiber axis was much less pronounced even 30  $\mu\text{m}$  into tendon than at the surface. Optical clearing could enable these measurements to be performed deeper into tissue. Moreover, we have previously demonstrated that 50% glycerol treatment of striated muscle did not affect the polarization profile relative to the control tissue.<sup>14</sup>

Our *ex vivo* results on improving the SHG signal collection through clearing suggest that this technique may be applicable *in vivo* as well (e.g., with sugar reagents). Such applications would require a backward-only collection scheme. The SHG directional data for muscle in Fig. 3(b) show that a large collection error will exist in the backward channel at imaging depths exceeding several MFPs (see, e.g., the control and 25% glycerol cleared tissue) due to the limited microscope collection aperture. Thus, an additional motivating factor for optical clearing lies in the enhanced photon collection from highly scattering turbid media in a backward-collection geometry for *in vivo* imaging.

## 5 Conclusions

SHG imaging in conjunction with optical clearing has great potential in terms of obtaining deeper penetration into tissues while maintaining all the structural information encoded in the signal. To further establish this method, we have examined the clearing mechanisms and capabilities in the two very different tissue types, striated muscle and tendon. The latter is essentially ECM, and the former is a cellular system linked by intercellular connective tissue. Given these structural dissimilarities, we find that the clearing mechanisms are indeed quite different. In tendon, the interfibril water is replaced by glycerol, resulting in decreased refractive index mismatch. In addition, due to the hyperosmolarity of glycerol, the interfibrillar spacing concurrently increases, increasing the distance between local scatterers. Both these effects result in a greatly reduced scattering coefficient, affording improved penetration into the tissue as well as reduced attenuation in the axial response of the SHG signal. The measured overall enhancement of the 3-D SHG intensity is in good agreement with the Monte Carlo simulations based on the measured bulk optical parameters. In the case of striated muscle, we find that the axial response is dominated by reduction of the primary filter. At the cellular level, optical clearing results from replacement of intracellular water with glycerol, permitting better refractive index matching with the surrounding perimysium and leading to significantly decreased scattering losses. The proportional decrease in  $\mu_s$  by treatment with fractional glycerol can be well-approximated by Mie theory. While differing in the details of their respective operative mechanisms, SHG imaging in conjunction with optical clearing of both tissue types results in improved depth of penetration as well as overall 3-D response and has great potential as a diagnostic imaging tool.

## Acknowledgments

We gratefully acknowledge support under NIH Grant No. EB-01842.

## References

1. A. G. Yodh and B. J. Tromberg, "Celebrating Britton Chance," *J. Biomed. Opt.* **5**(2), 115–118 (2000).
2. J. P. Culver, R. Choe, M. J. Holboke, L. Zubkov, T. Durduran, A. Slemph, V. Ntziachristos, B. Chance, and A. G. Yodh, "Three-dimensional diffuse optical tomography in the parallel plane transmission geometry: evaluation of a hybrid frequency domain/continuous wave clinical system for breast imaging," *Med. Phys.* **30**(2), 235–247 (2003).
3. A. E. Cerussi, A. J. Berger, F. Bevilacqua, N. Shah, D. Jakubowski, J. Butler, R. F. Holcombe, and B. J. Tromberg, "Sources of absorption and scattering contrast for near-infrared optical mammography," *Acad. Radiol.* **8**(3), 211–218 (2001).
4. X. Intes, C. Maloux, M. Guven, B. Yazici, and B. Chance, "Diffuse optical tomography with physiological and spatial *a priori* constraints," *Phys. Med. Biol.* **49**(12), N155–163 (2004).
5. B. W. Pogue, S. C. Davis, X. Song, B. A. Brookby, H. Dehghani, and K. D. Paulsen, "Image analysis methods for diffuse optical tomography," *J. Biomed. Opt.* **11**(3), 33001 (2006).
6. Q. Zhu, S. Tannenbaum, and S. H. Kurtzman, "Optical tomography with ultrasound localization for breast cancer diagnosis and treatment monitoring," *Surg. Oncol. Clin. N. Am.* **16**(2), 307–321 (2007).
7. M. H. Khan, B. Choi, S. Chess, K. M. Kelly, J. McCullough, and J. S. Nelson, "Optical clearing of *in vivo* human skin: implications for light-based diagnostic imaging and therapeutics," *Lasers Surg. Med.* **34**(2), 83–85 (2004).
8. M. H. Khan, S. Chess, B. Choi, K. M. Kelly, and J. S. Nelson, "Can topically applied optical clearing agents increase the epidermal dam-

- age threshold and enhance therapeutic efficacy?," *Lasers Surg. Med.* **35**, 93–95 (2004).
9. G. Vargas, E. K. Chan, J. K. Barton, H. G. Rylander III, and A. J. Welch, "Use of an agent to reduce scattering in skin," *Lasers Surg. Med.* **24**(2), 133–141 (1999).
  10. V. V. Tuchin, X. Q. Xu, and R. K. Wang, "Dynamic optical coherence tomography in studies of optical clearing, sedimentation, and aggregation of immersed blood," *Appl. Opt.* **41**(1), 258–271 (2002).
  11. A. N. Bashkatov, E. A. Genina, Y. P. Sinichkin, V. I. Kochubey, N. A. Lakodina, and V. V. Tuchin, "Glucose and mannitol diffusion in human dura mater," *Biophys. J.* **85**(5), 3310–3318 (2003).
  12. X. Q. Xu, R. K. Wang, and J. B. Elder, "Optical clearing effect on gastric tissues immersed with biocompatible chemical agents investigated by near infrared reflectance spectroscopy," *J. Phys. D* **36**(14), 1707–1713 (2003).
  13. E. A. Genina, A. N. Bashkatov, Y. P. Sinichkin, and V. V. Tuchin, "Optical clearing of the eye sclera *in vivo* caused by glucose," *Quantum Electron.* **36**(12), 1119–1124 (2006).
  14. S. Plotnikov, V. Juneja, A. B. Isaacson, W. A. Mohler, and P. J. Campagnola, "Optical clearing for improved contrast in second harmonic generation imaging of skeletal muscle," *Biophys. J.* **90**(1), 328–339 (2006).
  15. V. V. Tuchin, "Optical clearing of tissues and blood using the immersion method," *J. Phys. D* **38**(15), 2497–2518 (2005).
  16. A. T. Yeh and J. Hirshburg, "Molecular interactions of exogenous chemical agents with collagen—implications for tissue optical clearing," *J. Biomed. Opt.* **11**(1), 014003 (2006).
  17. J. Hirshburg, B. Choi, J. S. Nelson, and A. T. Yeh, "Correlation between collagen solubility and skin optical clearing using sugars," *Lasers Surg. Med.* **39**(2), 140–144 (2007).
  18. E. C. Rothstein, S. Carroll, C. A. Combs, P. D. Jobsis, and R. S. Balaban, "Skeletal muscle NAD(P)H two-photon fluorescence microscopy *in vivo*: topology and optical inner filters," *Biophys. J.* **88**(3), 2165–2176 (2005).
  19. W. Mohler, A. C. Millard, and P. J. Campagnola, "Second harmonic generation imaging of endogenous structural proteins," *Methods* **29**(1), 97–109 (2003).
  20. A. T. Yeh, N. Nassif, A. Zoumi, and B. J. Tromberg, "Selective corneal imaging using combined second-harmonic generation and two-photon excited fluorescence," *Opt. Lett.* **27**, 2082–2084 (2002).
  21. A. Zoumi, X. Lu, G. S. Kassab, and B. J. Tromberg, "Imaging coronary artery microstructure using second-harmonic and two-photon fluorescence microscopy," *Biophys. J.* **87**(4), 2778–2786 (2004).
  22. S.-P. Tai, T.-H. Tsai, W.-J. Lee, D.-B. Shieh, Y.-H. Liao, H.-Y. Huang, K. Zhang, H.-L. Liu, and C.-K. Sun, "Optical biopsy of fixed human skin with backward-collected optical harmonics signals," *Opt. Express* **13**, 8231–8242 (2005).
  23. S. J. Lin, S. H. Jee, C. J. Kuo, R. J. Wu, W. C. Lin, J. S. Chen, Y. H. Liao, C. J. Hsu, T. F. Tsai, Y. F. Chen, and C. Y. Dong, "Discrimination of basal cell carcinoma from normal dermal stroma by quantitative multiphoton imaging," *Opt. Lett.* **31**(18), 2756–2758 (2006).
  24. R. M. Williams, W. R. Zipfel, and W. W. Webb, "Interpreting second-harmonic generation images of collagen I fibrils," *Biophys. J.* **88**(2), 1377–1386 (2005).
  25. J. Reichman, , "Determination of absorption and scattering coefficients for nonhomogeneous media. 1: Theory," *Appl. Opt.* **12**, 1811–1815 (1973).
  26. H. Li and S. Xie, "Measurement method of the refractive index of biotissue by total internal reflection," *Appl. Opt.* **35**, 1793–1795 (1996).
  27. R. Marchesini, A. Bertoni, S. Andreola, E. Melloni, and A. E. Sichirollo, "Extinction and absorption coefficients and scattering phase functions of human tissues *in vitro*," *Appl. Opt.* **28**, 2318–2324 (1989).
  28. L. Wang, S. L. Jacques, and L. Zheng, "MCML—Monte Carlo modeling of light transport in multi-layered tissues," *Comput. Methods Programs Biomed.* **47**(2), 131–146 (1995).
  29. R. Lacombe, O. Nadiarykh, S. S. Townsend, and P. J. Campagnola, "Phase matching considerations in second harmonic generation from tissues: effects on emission directionality, conversion efficiency, and observed morphology," *Opt. Commun.* **281**, 1823–1832 (2008).
  30. O. Nadiarykh, R. B. LaComb, P. J. Campagnola, and W. A. Mohler, "Coherent and incoherent SHG in fibrillar cellulose matrices," *Opt. Express* **15**, 3348–3360 (2007).
  31. S. V. Plotnikov, A. C. Millard, P. J. Campagnola, and W. A. Mohler, "Characterization of the myosin-based source for second-harmonic generation from muscle sarcomeres," *Biophys. J.* **90**(2), 693–703 (2006).
  32. F. Legare, C. Pfeffer, and B. R. Olsen, "The role of backscattering in SHG tissue imaging," *Biophys. J.* **93**(4), 1312–1320 (2007).
  33. H. E. Huxley and J. Hanson, "Quantitative studies on the structure of cross-striated myofibrils. I. investigations by interference microscopy," *Biochim. Biophys. Acta* **23**(2), 229–249 (1957).
  34. J. Hanson and H. E. Huxley, "Quantitative studies on the structure of cross-striated myofibrils. II. investigations by biochemical techniques," *Biochim. Biophys. Acta* **23**(2), 250–260 (1957).
  35. R. Lacombe, O. Nadiarykh, and P. J. Campagnola, "SHG imaging of *osteogenesis imperfecta*: experiment and simulation," *Biophys. J.* (in press).
  36. A. J. Welch, C. Gardner, R. Richards-Kortum, E. Chan, G. Criswell, J. Pfefer, and S. Warren, "Propagation of fluorescent light," *Lasers Surg. Med.* **21**(2), 166–178 (1997).
  37. A. T. Yeh, B. Choi, J. S. Nelson, and B. J. Tromberg, "Reversible dissociation of collagen in tissues," *J. Invest. Dermatol.* **121**(6), 1332–1335 (2003).
  38. P. Stoller, B.-M. Kim, A. M. Rubinchik, K. M. Reiser, and L. B. Da Silva, "Polarization-dependent optical second-harmonic imaging of a rat-tail tendon," *J. Biomed. Opt.* **7**, 205–214 (2001).